

# Influence of the overlapped area on the corrosion behaviour of laser treated aluminium alloys

K.G. Watkins <sup>a,\*</sup>, Z. Liu <sup>a</sup>, M. McMahon <sup>b</sup>, R. Vilar <sup>c</sup>, M.G.S. Ferreira <sup>c</sup>

<sup>a</sup> Department of Mechanical Engineering, Brownlow Street, University of Liverpool, Liverpool L69 3GH, UK

<sup>b</sup> PASTIS-CNRSM, Brindisi, Italy

<sup>c</sup> Instituto Superior Tecnico, Lisbon, Portugal

Received 9 June 1997; received in revised form 18 August 1997

## Abstract

Laser surface treatments offer significant potential for improvement of materials properties such as corrosion performance and wear resistance. In large area applications, overlapping of individual tracks corresponding to the width of the laser beam is often required. This involves the heat treatment of a region adjacent to the previous track with microstructural changes such as precipitate coarsening and microsegregation at the overlap regions, which can lead to detrimental effects on the corrosion performance. This paper reports the characteristics and corrosion behaviour of the overlapped areas in the laser melting and alloying with Cr, W, Zr–Ni or Ti–Ni of 2014 aluminium alloy. It is shown that microsegregation occurs within the planar front zone of laser melted samples and microstructural coarsening occurs in the heat affected zones caused by the reheating effect at the laser track overlaps. Electrochemical testing has indicated that microsegregation within the overlapped areas leads to initiation of pitting corrosion in most of these cases. © 1998 Elsevier Science S.A. All rights reserved.

*Keywords:* Laser melting; Laser alloying; Overlapped area; Corrosion behaviour; Aluminium alloys

## 1. Introduction

There has been a significant level of investigation of the effect of laser surface melting (LSM) in modifying the microstructure of aluminium alloys [1–13]. This includes a growing number of studies of the influence of LSM on the corrosion properties of aluminium alloys [14–20]. Similarly, laser surface alloying (LSA) of aluminium alloys for enhancement of corrosion performances has received considerable attention [21], including work from laboratories [22–27]. A recent review summarising work in this area has been published [28].

Though most of the work concerning corrosion studies has demonstrated modest improvement in properties as a result of LSM and more significant improvements as a result of LSA, most authors have sought to emphasize the feasibility of improvements as a result of these methods and little attention has been given to the

requirements of area coverage as required in real engineering applications. All of this work has been carried out using carbon dioxide lasers of moderate power (1–5 kW) producing laser melt tracks of width 1–5 mm. Production of area coverage under these conditions necessitates the overlapping of adjacent tracks as a result of multiple passes of the laser. Under these conditions, the overlap zone between adjacent tracks will be subject to an additional heat treatment effect not received by the track centres, which may result in differences in microstructure between the track overlaps and the track centres. While this is unlikely to be a difficulty in the case of the production of wear resistant surfaces by LSM or LSA (where, indeed, the existence of harder and softer regions on the surface may be an advantage in terms of the entrapment of wear debris), corrosion performance is very sensitive to surface inhomogeneity.

The purpose of this paper is to summarise some of the effects of track overlap on the microstructure and corrosion performance of LSM and LSA of aluminium alloys and to point to the conclusion that solutions to

\* Corresponding author. Tel.: +44 151 7944820; fax: +44 151 7944892; e-mail: kwatkins@mechnet.liv.ac.uk

the problems identified are required if the state of the art is to proceed beyond the stage of the production of specimens to the surface enhancement of real engineering structures.

## 2. Experimental procedure

The aluminium alloy substrate material was aluminium alloy 2014-T6 (Al–4.65Cu–0.5Mg–0.8Si wt.%). The laser used was an Electrox 2 kW cw CO<sub>2</sub> laser. Ar gas shrouding was used to protect the surfaces from oxidation.

### 2.1. Laser melting

The aluminium alloy samples were pretreated to produce blackened surfaces to increase the absorptivity by coating with soot or by immersion in 20% NaOH solution for 10 min. The typical power density used was  $3.2 \times 10^5 \text{ W cm}^{-2}$  (i.e. power,  $P = 1600 \text{ W}$ , beam spot size,  $D = 0.8 \text{ mm}$ ) and the traverse speed of the workpiece beneath the laser beam was varied from  $2 \text{ mm s}^{-1}$  to  $180 \text{ mm s}^{-1}$ . The track overlap was 50%.

### 2.2. Laser alloying

Aluminium alloy substrates were precoated with the following coating types by plasma spraying: (a) 25Cr–75Al (90  $\mu\text{m}$ ); (b) 75Cr–25Al (90  $\mu\text{m}$ ); (c) 25W–75Al (90  $\mu\text{m}$ ); (d) 75W–25Al (90  $\mu\text{m}$ ); (e) 8Al–72Zr–20Ni (80  $\mu\text{m}$ ); or (f) 35Al–50Ti–15Ni (80  $\mu\text{m}$ ). All compositions are in weight per cent and the nominal coating thickness is shown in parenthesis.

The power density was  $8.5 \times 10^4 \text{ W cm}^{-2}$  ( $P = 1450 \text{ W}$  and  $D = 1.5 \text{ mm}$ ) for coating types (a)–(d) and  $2.9 \times 10^5$  ( $P = 1450 \text{ W}$  and  $D = 0.8 \text{ mm}$ ) for coating types (e) and (f). A two-step process was applied: The aim of the first step, laser pretreatment, was to obtain compositionally homogeneous alloyed layers. The second step, laser remelting, was required to remelt the pretreated alloyed surfaces with faster traverse speeds to obtain faster cooling rate and to eliminate the porosity formed in the first step process. For laser alloying of Cr and W (coating types (a)–(d)), the traverse speed of the first step was varied from 5 to  $50 \text{ mm s}^{-1}$  and the speed of the second step was  $50 \text{ mm s}^{-1}$ . The overlap rate was kept constant at 50%. For laser alloying of Zr–Ni and Ti–Ni, (coating types (e) and (f)) the traverse speed of the first step was  $60 \text{ mm s}^{-1}$  and five different overlapping ratios were applied from 25 to 75%. The traverse speeds of the second step were 200, 250 and  $300 \text{ mm s}^{-1}$ , respectively and the overlapping rate in this remelting step was kept constant at 40%.

Characterisation of the microstructure was performed by optical microscopy (following metallo-

graphic preparation and etching with a solution of 0.5% HF or a mixture of 3% HF, 6% HNO<sub>3</sub> and 91% distilled water), SEM and TEM. Compositional analysis of selected samples was performed using EDAX and EPMA. Electrochemical behaviour of the laser treated samples was studied in deaerated 1 M NaCl solution at 30°C. All the samples were tested after subsequent polishing to 1200 grit with emery paper and 3  $\mu\text{m}$  diamond paste in order to present a uniform surface roughness. The area to be examined, which was between 0.18 and 0.37  $\text{cm}^2$ , was isolated by masking with Alcomit lacquer. The solutions were deaerated by bubbling nitrogen gas through the solution for at least 90 min. The relative steady open circuit potential was recorded after the samples were immersed in the solution for at least 2 h. Anodic polarisation curves were determined potentiodynamically with a potential scan rate of  $10 \text{ mV min}^{-1}$  using a Sycopel 251 computer controlled potentiostat and a conventional three-electrode cell employing a platinised titanium counter electrode and a saturated calomel reference electrode (SCE).

## 3. Results and discussion

### 3.1. Microstructural studies

#### 3.1.1. LSM of 2014 aluminium alloy

After laser melting of the 2014 aluminium alloy, the microstructure consisted of columnar grains that had grown epitaxially from the unmelted substrate as shown in Fig. 1. At the fusion boundary there was a thin planar front zone (PFZ) of thickness 3–5  $\mu\text{m}$  in contact with the substrate, extending from the bottom of the melt track up to the surface and then intersecting the adjacent melt pool periphery. Beyond this interface, the structure was cellular–dendritic. Such microstructures

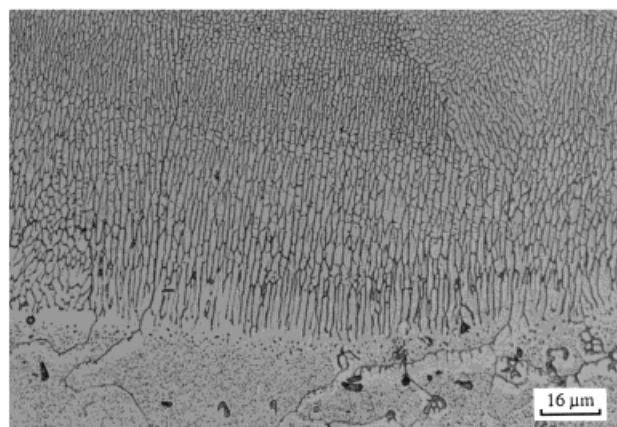


Fig. 1. PFZ and columnar grains formed by epitaxial solidification for the LSM 2014 Al alloy ( $P = 1600 \text{ W}$ ,  $D = 0.8 \text{ mm}$  and  $v = 30 \text{ mm s}^{-1}$ ).

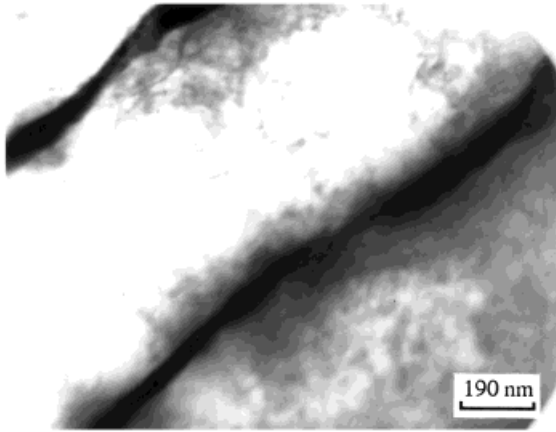


Fig. 2. TEM micrograph of  $\alpha$ -Al dendrites in the inner part of the LSM 2014 Al alloy ( $P = 1600$  W,  $D = 0.8$  mm and  $v = 30$  mm s<sup>-1</sup>).

are clearly in accord with the calculated high initial ratio of thermal gradient and solidification rate and its fall-off as solidification proceeds towards the free surface. Fig. 2 shows a TEM micrograph of dendrites in the centre of the melted track. The wider and lighter phase is an  $\alpha$ -Al solid solution whereas the precipitates are confined to the dendritic boundaries as the darker line.

A significant feature of the microsegregation was discovered in the planar front fusion zone. Fig. 3 shows the Cu distribution map measured by EMPA in the PFZ with the corresponding microstructures, which shows that Cu concentration was lower near the fusion line and then increased toward the interface with the cellular–dendritic zone. Cu concentration in the PFZ was about 2.5 wt%, which is lower than the equilibrium value (4.65 wt%) of the untreated substrate. This phenomenon was also investigated by Munitz [4] for Al–Cu alloys. Microsegregation such as cellular, dendritic and grain boundary segregation can also occur during solidification when solute is rejected at the interface and a boundary layer enriched in solute builds up in the liquid immediately ahead of the solidification front. Enrichment of the solute at the liquid–solid interface during solidification results in the formation of the precipitates in the interdendritic spaces. As a result Cu was depleted in the dendritic matrix.

Another segregation pattern observed is solute banding which was revealed on etching as light and dark regions marking successive positions of the advancing interface. The contrast is caused by periodic regions of solute enrichment or depletion revealed on etching and indicates the sudden change of the local growth rate. By analysing copper concentration across several bands, it was found that the copper is more concentrated at transitions in the microstructure bands.

Fig. 4 shows a surface view of overlapped tracks. It was found that the PFZs were present on the surface

between the tracks due to the PFZs extending from the bottom of the melt track to the surface and the intersecting the adjacent melt track. Fig. 5 shows the microstructure of the heat affected zone (HAZ) caused by overlapping. It can be seen that in the HAZ the dendrites have recrystallised and that granular growth has occurred to some extent by the reheating effect which allows the interdendritic phase to transform to blocky second phase particles. In addition, the corresponding grain boundaries were also thicker than those in the unaffected melt zone.

### 3.1.2. LSA of 2014 alloy with Cr and W

After LSA, a heterogeneous microstructure was found due to the features of solidification. For LSA of 2014 aluminium alloy with Cr, it was found [26] that

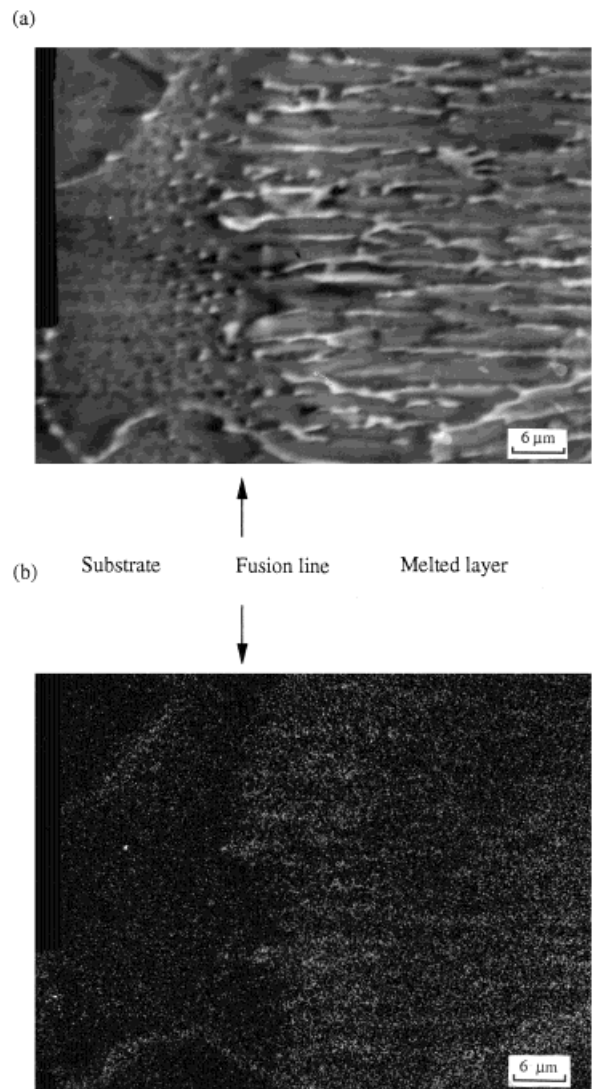


Fig. 3. Cu distribution map in the planar front fusion zone in LSM 2014 Al alloy ( $P = 1600$  W,  $D = 0.8$  mm and  $v = 30$  mm s<sup>-1</sup>). (a) SEM photograph of the planar front zone; (b) Cu distribution map in the corresponding zone.

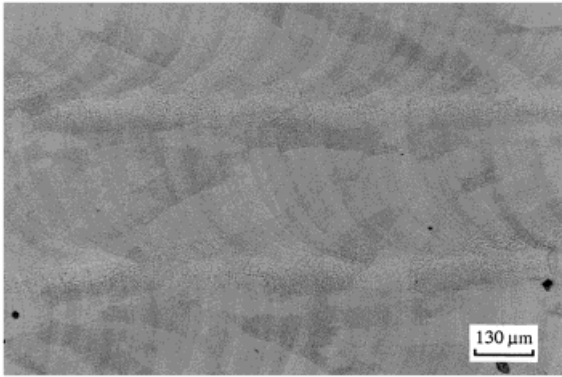


Fig. 4. Surface view of the overlapped tracks on LSM 2014 Al alloy ( $P = 1600$  W,  $D = 0.8$  mm,  $v = 40$  mm s<sup>-1</sup> and overlap rate = 50%)

fine complex-shaped Cr–Al intermetallics were distributed in the  $\alpha$ -Al solid solution at the inner part of the tracks and coarse needle-shaped intermetallics were present at the edge of the melt pool corresponding to the overlapped region. The PFZ was not observed at the surface. The content of Cr in the  $\alpha$ -Al measured by EPMA was 0.6 at.%, which is higher than the equilibrium solubility of 0.38 at.%. A similar microstructure was found in W alloyed layers as shown in Fig. 6. It was found that there was a difference of microstructure between the inner part of the tracks and the overlapped regions which had coarser blocky Al–W precipitates.

### 3.1.3. LSA of 2014 alloy with Zr–Ni and Ti–Ni

Figs. 7 and 8 show the typical microstructure of laser alloyed Zr–Ni and Ti–Ni samples, respectively. It was observed that both of the alloys exhibited a very thin glass-like layer (3–5  $\mu$ m) on the top surface beneath which was a dendritic solidification structure. These thin layers did not reveal any crystalline features after heavy etching. From SEM observations, it was judged

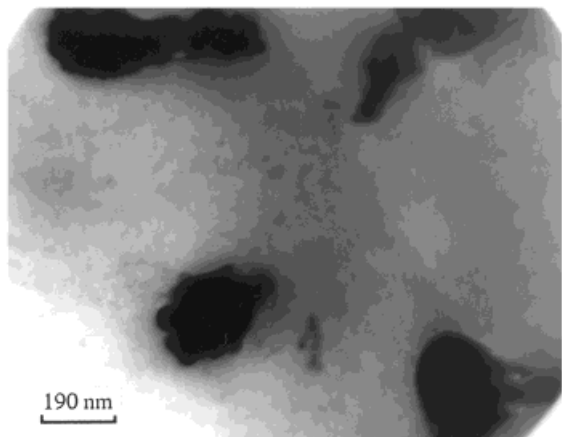
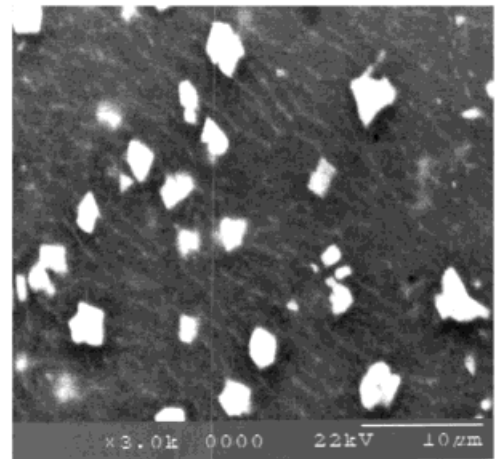


Fig. 5. TEM micrograph of microstructure in the HAZ of LSM 2014 Al alloy ( $P = 1600$  W,  $D = 0.8$  mm,  $v = 40$  mm s<sup>-1</sup> and overlap rate = 50%).



(a)



(b)

Fig. 6. SEM micrographs of LSA 2014/W alloy showing microstructural difference between the inner (a) and the overlapped (b) regions.

that this could be an amorphous phase and this was partially confirmed by XRD [24]. It was also found that these layers did not cover the whole surface. It appeared (see Fig. 9) that for Al–Zr–Ni, the microstructure at the surface in the centre of the laser tracks consisted of a non-crystalline phase but at the track overlaps microcrystalline structures were formed. This could be due to the reheating process at track overlaps or non-uniform distribution of cooling effect within the melt pool of each track.

## 3.2. Corrosion behaviour

### 3.2.1. Laser melting

Fig. 10 shows polarisation curves which indicate the breakdown potentials of the samples before and after laser melting treatment. For the untreated alloy, the breakdown potential was  $-715$  mV while after CO<sub>2</sub> laser melting, the breakdown potential was  $-550$  mV. This represents an increase in breakdown potential of 165 mV for CO<sub>2</sub> laser melting treatment compared with

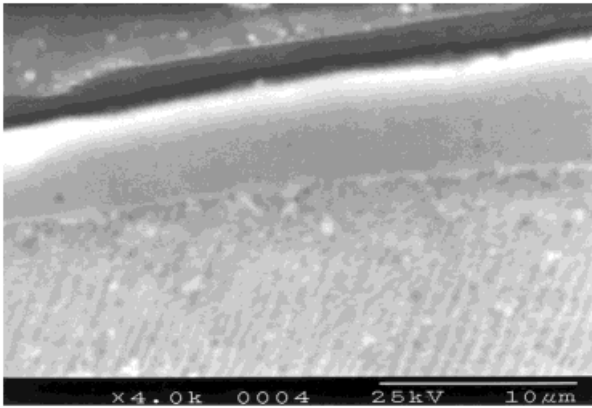


Fig. 7. SEM micrograph of cross section of LSA 2014/Zr–Ni alloy (first step:  $P = 1450$  W,  $D = 0.8$  mm,  $v = 25$  mm s<sup>-1</sup> and overlap rate = 50%; second step:  $P = 1450$  W,  $D = 0.8$  mm,  $v = 250$  mm s<sup>-1</sup> and overlap rate = 40%).

the as-received alloy. Following polarization beyond the breakdown potential, the as-received alloy presented irregular deep pits. However, for the case of CO<sub>2</sub> laser melting under the same conditions, four types of corrosion mechanism attributed to segregation were found, as shown in Fig. 11.

(i) Corrosion along the planar front fusion zone: Cu concentration was lower where the PFZ met the surface at the track overlaps, resulting in inter-track corrosion initiation. It was also interesting to note that the corrosion eventually encountered the HAZ caused by reheating at track overlaps where precipitate coarsening takes place. It is difficult to determine whether pits are initiated in the planar front zone or the HAZ, or simultaneously in both areas, however it is most likely that they initiate in the planar front zone and develop further towards the HAZs.

(ii) Pitting in the cellular and dendritic zone: The microsegregation of Cu in cellular and dendritic

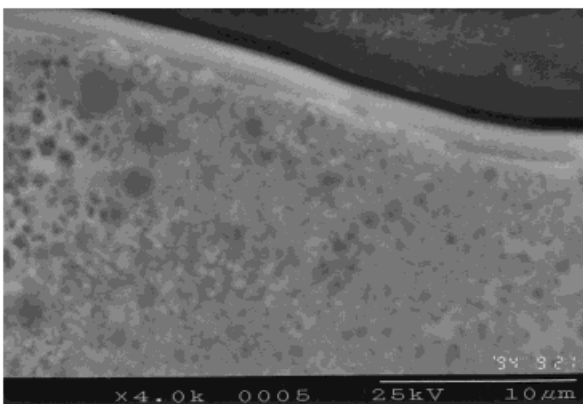


Fig. 8. SEM micrograph of cross section of LSA 2014/Ti–Ni alloy (first step:  $P = 1450$  W,  $D = 0.8$  mm,  $v = 30$  mm s<sup>-1</sup> and overlap rate = 50%; second step:  $P = 1450$  W,  $D = 0.8$  mm,  $v = 300$  mm s<sup>-1</sup> and overlap rate = 40%).

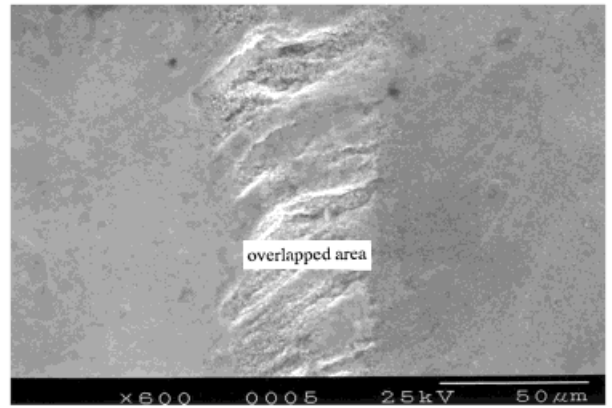


Fig. 9. SEM micrograph of surface view of LSA 2014/Zr–Ni alloy (first step:  $P = 1450$  W,  $D = 0.8$  mm,  $v = 25$  mm s<sup>-1</sup> and overlap rate = 50%; second step:  $P = 1450$  W,  $D = 0.8$  mm,  $v = 250$  mm s<sup>-1</sup> and overlap rate = 40%).

boundaries resulted in pitting initiation in the dendritic matrix. It seemed that the pitting followed the cell orientation.

(iii) Corrosion along the grain boundaries or intergranular cracks: The formation of precipitates at grain boundaries resulted in Cu depletion regions surrounding the precipitates with pitting taking place preferentially along the grain boundaries. This was often the case when intergranular cracks were present in the melted surfaces.

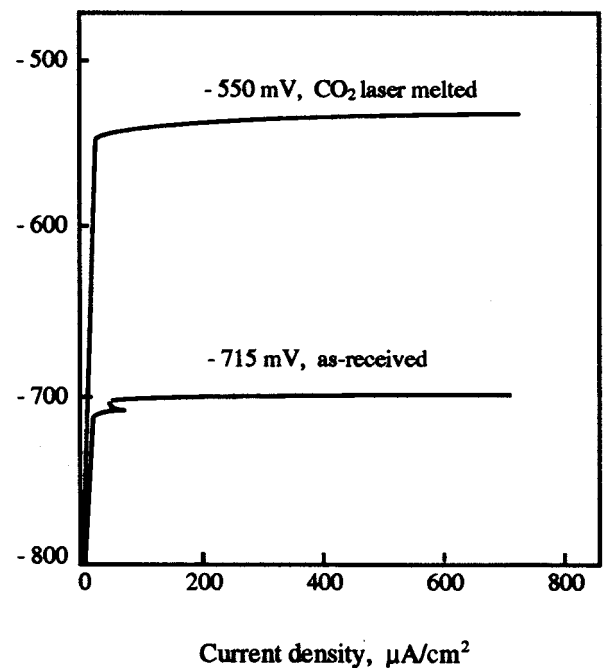


Fig. 10. Polarisation curves of the 2014 Al alloy before and after LSM ( $P = 1600$  W,  $D = 0.8$  mm,  $v = 40$  mm s<sup>-1</sup> and overlap rate = 50%). Tested in 1 M NaCl solution at 30°C, deaerated for 2 h with N<sub>2</sub>, 10 mV min<sup>-1</sup>.

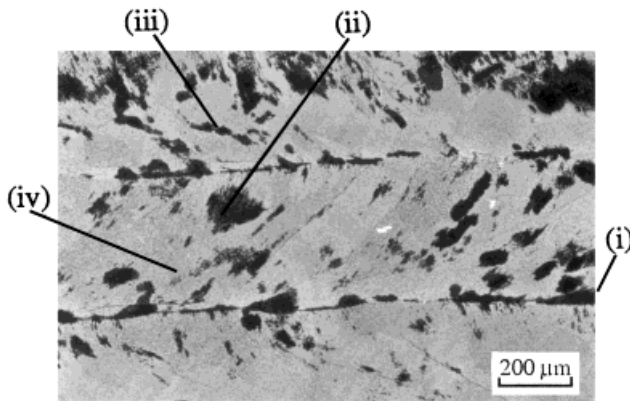


Fig. 11. Pitting morphology and distribution of LSM 2014 Al alloy after polarisation.

(iv) Pitting in the banding structure: Some pits were found in the solute banding structures, but this did not appear to be the main contributor to the corrosion performance.

These observations indicate that copper segregation markedly influences pitting behaviour, the highest pitting susceptibility occurring in the regions of minimum Cu concentration. This is consistent with the observation of the pitting corrosion of segregated Al–Cu alloys by Yasuda et al. [29], where the pitting potential and pitting sites are determined solely by the regions of the most severe solute depletion. In our study, observation of the polarised samples indicated that pitting of types (i), (ii) and (iii) dominated the corrosion behaviour of the LSM 2014 alloy. Solute banding was not a main site for pitting initiation. However, free corrosion immersion in 1M NaCl solution for 150 h indicated (see Fig. 12) that most of the pit sites coincided with track overlaps suggesting that pitting in the PFZ is predominant in determining the pitting behaviour. Corrosion behaviour of the melted surfaces with fast traverse speeds was still dominated by pitting of types (i) and (ii) with pitting at intergranular cracks playing an addi-

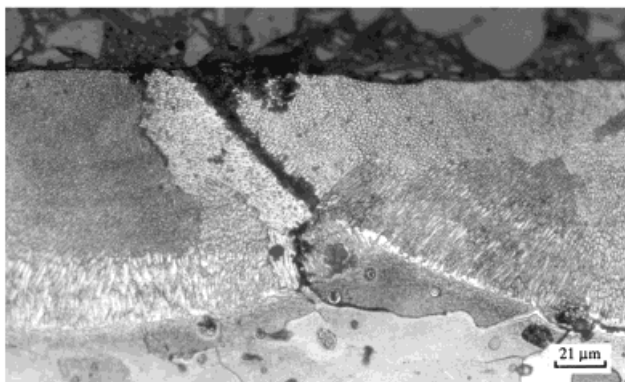


Fig. 12. Cross section of the LSM 2014 Al alloy ( $P=1600$  W,  $D=0.8$  mm  $s^{-1}$ ,  $v=40$  mm  $s^{-1}$  and overlap rate = 50%) after immersion test in 1 M NaCl solution at 30°C for 150 h.

tional role. Higher melting speed resulted in finer dendritic structures, but pitting in the dendritic matrix still occurred.

The selective dissolution of overlap regions has also been revealed on the laser melted surfaces of other alloys. Virtanen and Böhni [19,20] reported that laser surface melting of Al–Si alloys can significantly improve the pitting resistance. Alloys with up to 12% Si exhibit a significantly higher pitting potential after laser treatment, but if the Si content exceeds 17% the laser treated surface exhibits more heterogeneity, especially in the interface regions of neighbouring laser tracks, which show less resistance to pitting. Selective dissolution of the interface regions of the neighbouring laser tracks was found in laser surface modification of Fe–10Cr–13P–7C alloy due to a much coarser microstructure and a stronger segregation at the interface regions than the inner part of the tracks. It was also observed by Escudero and Bello [13] that for laser surface melting of martensitic stainless steel AISI 420, the edge zones affected by the laser treatment and the overlapping areas of successive laser runs were the more corrosion sensitive regions. The pits were aligned along the edge of the laser track or within the run overlap area.

The increase of the breakdown potential of the 2014 aluminium alloy as a result of LSM could be accounted for in the effect of the refined microstructure produced on the mechanism of pitting in chloride electrolytes. Before laser treatment, 2014–T6 aluminium alloys contain large second phase particles in the surface which are preferred sites for  $Cl^-$  adsorption and subsequent pitting initiation. After laser melting, a larger number of possible sites for pitting are produced, but because the second phase particles are smaller, the breakdown of the oxide film would be more difficult, since there would be less localised thinning of the oxide layer over the smaller particles. However, Cu depleted areas can promote localised attack due to the formation of local electrochemical cells caused by the difference in potential with the matrix. Al is anodic to Cu and hence Al corrodes preferentially. Once pits are initiated in the PFZ, they further develop towards the HAZ as a result of coarsened second phase particles in this region.

Hence,  $CO_2$  laser surface melting of 2014 alloy can improve pitting resistance, but the extent of improvement is limited due to Cu segregation and by the fact that no fundamental change in the chemical composition of the surface by addition of more corrosion resistant elements is possible, as in laser surface alloying.

### 3.2.2. Laser alloying

The pitting potentials,  $E_p$ , for various laser alloyed samples are shown in Table 1. Compared with the as-received 2014 alloy,  $E_p$  values were shifted positively by

Table 1  
Pitting potentials of various alloyed samples

Samples	Pitting potential (mV), $E_p$
2014 as received	-715
Cr alloyed (25Cr-75Al)	-500
Cr alloyed (75Cr-25Al)	-496
W alloyed (25W-75Al)	-597
W alloyed (75W-25Al)	-604
Al-Zr-Ni alloyed	-465
Al-Ti-Ni alloyed	-265

The initial coating composition (wt.%) is shown in parentheses.

all alloying additions. Further investigation of pit morphologies and distribution indicated that pits were initiated in different locations depending on LSA type.

For Al-Cr alloyed surfaces, an improvement in  $E_p$  of 219 mV was achieved, compared with the untreated 2014 alloy. As a result of anodic polarisation, numerous pits were observed because of the high anodic potential reached by the sample (Fig. 13). However, some of the pits found were caused by the reheating effect at track overlaps where the pits presented a semicircular profile. It appeared that the pits formed in the HAZ were hindered by the interfaces between the tracks.

Fig. 14 a shows the surface morphology of W alloyed layers after polarisation where the applied potential was stopped just after pitting occurred. It can be seen that most of the pit sites were preferentially formed at the overlaps and further developed by propagating along the track overlap close to the HAZ. More prolonged polarisation at higher anodic potential resulted in more extensive pitting at the track overlaps, as shown in Fig. 14 b.

The critical pitting potential of laser alloyed Al-Zr-Ni was -465 mV, showing an increase of 250 mV compared with as-received 2014 aluminium alloy. The surface morphology of the laser treated layers after

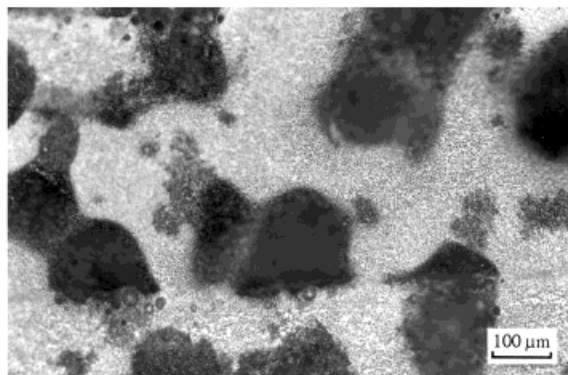
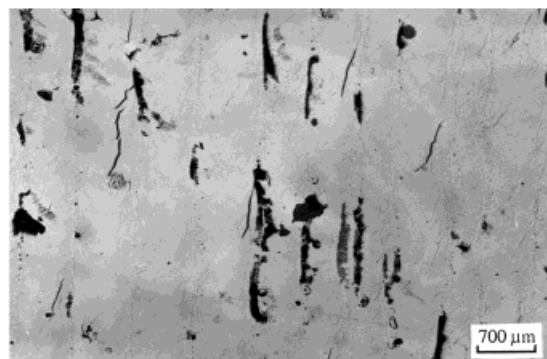
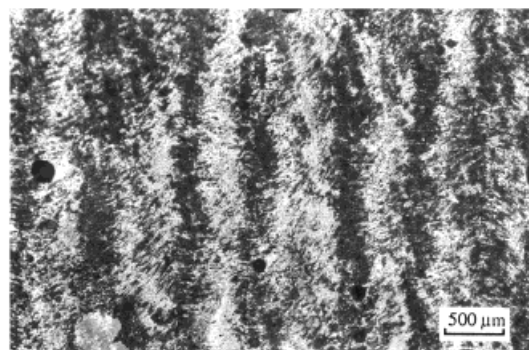


Fig. 13. Pitting morphology of LSA 2014/Cr alloy after polarisation. Tested in 1 M NaCl solution at 30°C, deaerated for 2 h with  $N_2$ , 10 mV min<sup>-1</sup>.



(a)



(b)

Fig. 14. Pitting morphology and distribution of the LSA 2014/W alloy. Tested in 1 M NaCl solution at 30°C, deaerated for 2 h with  $N_2$ , 10 mV min<sup>-1</sup>. (a) just after pitting occurred; (b) after further polarisation.

polarisation showed that some deep pits were located in the overlap regions, but pits were also found in other areas, making it difficult to assess the role of track overlap in this case. For Al-Ti-Ni alloys, pitting potential increased with overlapping rate. This represented the influence of microstructural changes produced by the reheating induced by overlapping which resulted in increase in the amount of  $\alpha$ -Ti and suggested that within the inherent improvement of the pitting potential for Al-Ti-Ni compared with the as-received 2014 aluminium alloy, the closer equilibrium phases produced at high degree of overlap were most favourable. The best pitting potential of laser alloyed Al-Ti-Ni alloys was -265 mV, showing an increase of 450 mV compared with the as-received 2014 aluminium alloy. The surface morphology of polarised surfaces did not show a selective dissolution at the interfaces.

Recent investigations of corrosion behaviour of single phase Al-M (transition metals) solid solutions produced using nonequilibrium alloying methods (RF sputtering) have led to a new understanding of the pitting corrosion mechanism [30]. The mechanism of passivity enhancement for these alloys appears to involve modification of the passive film structure to form a more protective barrier to oxygen and chloride transport. For instance, CrOOH or Cr<sub>2</sub>O<sub>3</sub> on an Al-Cr

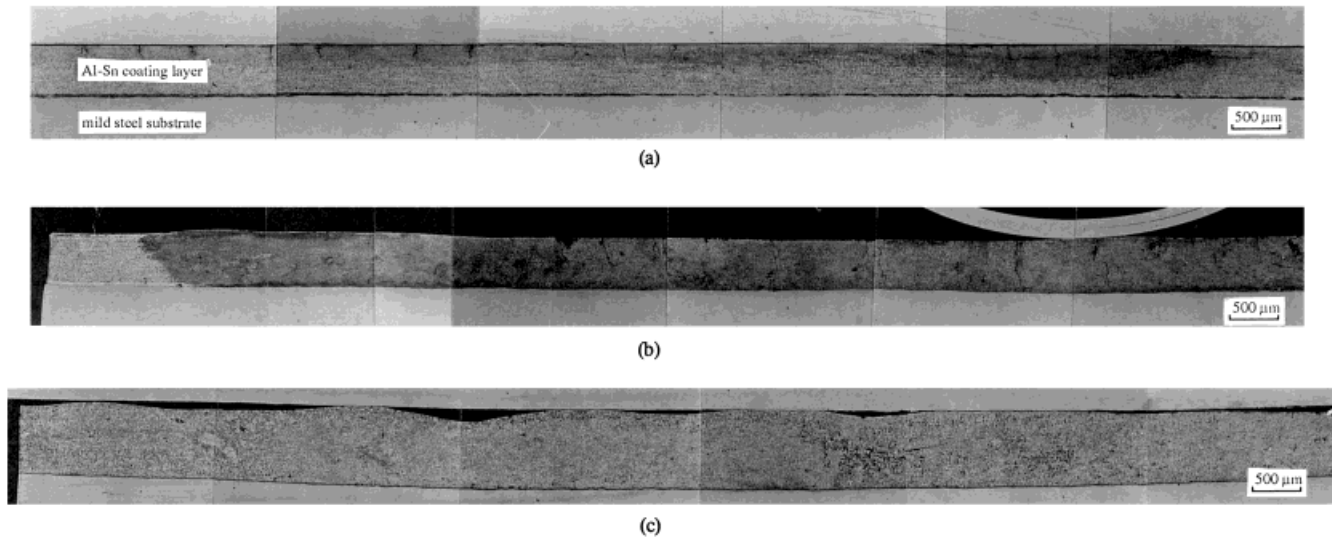


Fig. 15. Cross sections of the wide beam melted layers of a 500  $\mu\text{m}$  thick Al–Sn alloy coating on steel of thickness 2 mm (power = 10 kW, beam width = 30 mm). (a)  $v = 72 \text{ mm s}^{-1}$ ; (b)  $v = 60 \text{ mm s}^{-1}$ ; (c)  $v = 45 \text{ mm s}^{-1}$ .

surface is less soluble and more protective compared with an  $\text{Al}_2\text{O}_3$  film, resulting in a more positive pitting potential. It was also reported [31] that the small amount of the oxidised form of the solute W in the form of  $\text{WO}_2$  and  $\text{WO}_3$  (or  $\text{WO}_4^{2-}$ ) in the passive film may interact synergistically with the hydrated aluminium oxide structure to form a more protective film. For Al–Zr alloys, only one oxidised form of the solute  $\text{ZrO}_2$  is present within the film. These mechanisms are based on the fact that all the elements are retained in solid solution. However, in the present study, formation of a single phase solid solution was not achieved in the various laser alloyed samples. Once precipitates are formed in aluminium matrices, galvanic microcells are produced between these precipitates and the aluminium matrix due to difference in potential, resulting in selective attack. For the W alloyed surfaces, selective dissolution at interfaces clearly dominated the corrosion performance. For the other three alloys however, this phenomenon was less pronounced. This could be connected with the existence of a PFZ at the surface in Al–W alloy with the possibility of depletion of the amount of W in solid solution as a result of segregation effects at the overlap region.

### 3.3. Wide beam laser melting

A common feature of the various alloying treatments is the non-uniform attack on the laser treated surfaces. In particular, selective corrosion of the interface regions of neighbouring laser tracks takes place due to the increased segregation and coarser microstructure at the overlaps compared with the inner part of the tracks. In order to achieve a laser treated surface via melting or alloying with a high corrosion resistance, the generation

of a more homogeneous structure over the whole surface is required. One solution is the use of wide track melting or alloying using high power lasers.

Initial work on the use of 17 and 30 mm wide beams produced by cylindrical optics from a high power  $\text{CO}_2$  laser operating at 10–18 kW and with a substrate translation velocity of 33–133  $\text{mm s}^{-1}$  has been carried out at Fraunhofer ILT, Aachen, for the surface melting of a 500  $\mu\text{m}$  thick Al–Sn alloy coating on steel of thickness 2 mm. The results (Fig. 15) show that melting of the aluminium layer with controlled width and depth was successfully achieved. For instance (Fig. 15 a), when laser operating conditions of power = 10 kW, beam width = 30 mm and traverse speed = 72  $\text{mm s}^{-1}$  were applied, the aluminium layer was partially melted to a depth of 150  $\mu\text{m}$ . Some cracking was evident. At lower speeds (Fig. 15 b and c) less cracking was evident, but the melt depth was greater. The most important feature of this process is the generation of a uniform solidification microstructure in the melted layers. It is also interesting to note that planar front growth was not found and the melt zone consisted of a fully dendritic structure. Corrosion behaviour of the melted layer has yet to be investigated.

## 4. Conclusions

- (1) Production of a large processed area by overlapping results in segregation and coarsening of microstructure at the overlaps of the laser tracks.
- (2) Pitting resistance of  $\text{CO}_2$  laser melted 2014 alloys was increased compared with the as-received material. However, it appears that a selective dissolution of the interface regions of the laser tracks dominates the pitting behaviour.

(3) For W alloyed surfaces, a selective dissolution at interfaces dominated the corrosion performance, but for the other three alloys (Cr, Zr–Ni or Ti–Ni in aluminium) this phenomenon was less pronounced.

(4) Initial trials of wide beam melting of Al–Sn coated steel using a high power CO<sub>2</sub> laser have shown promising results.

### Acknowledgements

This work was carried out as a part of EC BRITE/EuRam Project BE-4305. The authors would like to thank Fraunhofer-Institut für Lasertechnik ILT, Aachen, for the use of a 25 kW CO<sub>2</sub> laser.

### References

- [1] G. Kaech, W. Epprecht, *Scripta Metall.* 12 (1978) 493.
- [2] C. Kimm, L.S. Weinman, *Scripta Metall. Mater.* 12 (1978) 57.
- [3] A. Munitz, *Metall. Trans. B* 11B (1980) 563.
- [4] A. Munitz, *Metall. Trans. B* 16B (1985) 149.
- [5] P. Reznicek, M. Holmanova, O. Honzik, *Aluminium* 65 (1989) 1259.
- [6] J.O. Milewski, G.K. Lewis, J.E. Wittig, *Weld. Res. Supp.* July, 1993, 341-s.
- [7] M. Zimmermann, M. Carrard, W. Kurz, *Acta Metall.* 37 (1989) 3305.
- [8] S.C. Gill, W. Kurz, *Acta Mater.* 41 (1993) 3563.
- [9] S.C. Gill, W. Kurz, *Mater. Sci. Eng.* A173 (1993) 335.
- [10] S.C. Gill, M. Zimmermann, W. Kurz, *Acta Metall. Mater.* 40 (1992) 2895.
- [11] H. Simidzu, S. Katayama, A. Matsunawa, in: S.L. Ream, F. Dausinger, T. Fujioka (Eds.), *Proceedings of the Conference of ICALEO 90, Florida, Laser Institute of America*, vol. 71, 1990, pp. 492.
- [12] S. Katayama, H. Muraki, H. Simidzu, A. Matsunawa, in: E.A. Metzbauer, E. Beyer, A. Matsunawa (Eds.), *Proceedings of the Conference of ICALEO 91, Florida, Laser Institute of America*, Vol 74, 1991, pp. 352.
- [13] M.L. Escudero, J.M. Bello, *Mater. Sci. Eng.* A158 (1992) 227.
- [14] P.G. Moore, E. McCafferty, L.S. Weinman, Report NRL Progress, November 1977, pp. 9.
- [15] P.L. Bonora, M. Bassoli, P.L. De Anna, G. Battaglin, G. Della Mea, P. Mazzoldi, A. Miotello, *Electrochim. Acta* 25 (1980) 1497.
- [16] P.L. Hagans, R.L. Yates, in: G.S. Was, K.S. Grabowski (Eds.), *Environmental Degradation of Ion and Laser Beam Treated Surfaces*, TMS, 1989, pp. 215.
- [17] E. McCafferty, P.G. Moore, G.T. Peace, *J. Electrochem. Soc.* 129 (1982) 9.
- [18] B.K. Opara, V.M. Andriyakhin, V.I. Volgin, V.V. Bandurkin, *Prot. Met. (USSR)* 21 (1985) 74.
- [19] S. Virtanen, H. Böhni, *Proceedings of the European Symposium on Modification of Passive Films*, Paris, France, 1993.
- [20] S. Virtanen, H. Böhni, R. Busin, T. Marchione, M. Pierantoni, E. Blank, *Corros. Sci.* 36 (9) (1994) 1623.
- [21] C.W. Draper, J.M. Poate, *Int. Met. Rev.* 30 (1985) 85.
- [22] Z. Liu, M. McMahon, K.G. Watkins, W.M. Steen, in: Y.F. Lu (Ed.), *Proceedings of the Conference of ISLOE 93: Singapore*, 1993, pp. 58.
- [23] K.G. Watkins, M.G. Ferreira, R. Vilar, W.M. Steen, Z. Liu, in: T.D. McCay, A. Matsunawa, H. Hügel (Eds.), in: *Proceedings of ICALEO 94: Laser Materials Processing*, Laser Institute of America, vol. 79, 1994, pp. 135.
- [24] Z. Liu, C.S. Xie, K.G. Watkins, W.M. Steen, in: J. Mazumder, A. Matsunawa, C. Magnusson (Eds.), *Proceedings of ICALEO 95: Laser Materials Processing*, San Diego, USA, Laser Institute of America, vol. 80, 1995, pp. 431.
- [25] M. McMahon, K.G. Watkins, M.G. Ferreira, R. Vilar, W.M. Steen, in: J. Mazumder, O. Conde, R. Vilar, W.M. Steen (Eds.) *Proceedings of the Conference of the NATO Advanced Study Institute on Laser Processing: Surface Treatment and Film Deposition*, Portugal, Series E: Applied Sciences, vol. 307, 1994, pp. 337.
- [26] A. Almeida, M. Anjos, R. Vilar, R. Li, M.G. Ferreira, K.G. Watkins, W.M. Steen, *Surf. Coat. Technol.* 70 (1995) 221.
- [27] R. Li, M.G.S. Ferreira, A. Almeida, R. Vilar, K.G. Watkins, M.A. McMahon, W.M. Steen, *Surf. Coat. Technol.* 81 (1996) 290.
- [28] K.G. Watkins, M.A. McMahon, W.M. Steen, *Mater. Sci. Eng.*, A231 (1997) 55.
- [29] M. Yasuda, F. Weinberg, D. Tromans, *J. Electrochem. Soc.* 137 (12) (1990) 3716.
- [30] G.S. Frenkel, R.C. Newman, C.V. Jahnes, M.A. Russak, *J. Electrochem. Soc.* 140 (1993) 2192.
- [31] B.A. Shaw, G.D. Davis, T.L. Fritz, B.J. Rees, W.C. Moshier, *J. Electrochem. Soc.* 138 (11) (1991) 3288.